# Magnetohydrodynamics approach for active decay heat removal system in future generation IV reactor

**Authors:** Lee, G., & Kim, H.R*.

**Journal Information:**

- **Journal:** International Journal of Energy Research
- **Year:** 2018
- **Volume:** 42(10)
- **Pages:** 3266-3278
- **DOI:** https://doi.org/10.1002/er.4080

---

# Magnetohydrodynamics approach for active decay heat removal system in future generation IV reactor

**Geun Hyeong Lee, Hee Reyoung Kim***

*Ulsan National Institute of Science and Technology, Ulsan 689-798, Republic of Korea*

## Abstract

In this work, a helical-type magnetohydrodynamics transportation system for active decay-heat-removal system in a prototype fourth-generation sodium fast reactor was numerically analysed considering operational conditions of atmospheric pressure, for liquid sodium transportation in a loop. The prototype fourth-generation sodium fast reactor is a reactor with high uranium utilisation and an electric power output of 150 MWe, subjected to a developed pressure of 10 kPa and flowrate of 0.005 $m^3/s$ under a temperature condition of 468.75 K for the active decay-heat-removal system. A helical-type magnetohydrodynamics transportation system was used to develop pressure in such a loop to reduce the current compared with that in a rectangular-type one; this could overcome the principal limitation of the requirement of a high current in a magnetohydrodynamics transportation system. The main parameters of the considered helical-type magnetohydrodynamics transportation system were: the inner diameter, silver brazing, number of turns, and radius of pump, which affect the current, magnetic-flux density, and its velocity. The parameters were analysed in relation to the minimisation of the pump current while maximising the pressure. The specifications of the optimised helical-type magnetohydrodynamics transportation system—current of 352 A and magnetic-flux density of 0.466 T—were derived to satisfy the conditions of the active decay-heat-removal system.

Keywords: ADHRS, helical-type MHD transportation system, magnetic-flux density, current.

## NOMENCLATURE

| | |
|---|---|
| $B$ | Magnetic-flux density [T] |
| $B_e$ | Magnetic-flux density from permanent magnet [T] |
| $B_i$ | Magnetic-flux density from electrode stub [T] |
| $B_t$ | Total magnetic-flux density [T] |
| $d$ | Inner diameter [m] |
| $D$ | Hydraulic diameter [m] |
| $E$ | Electric field [$kg \cdot m/(s^3 \cdot A)$] |
| $E_t$ | Total electric field [$kg \cdot m/(s^3 \cdot A)$] |
| $f$ | Force density [$kg/(s^2 \cdot m^2)$] |
| $f_d$ | Darcy friction factor |
| $f_r$ | Friction factor according to pipe diameter |
| $H$ | Magnetic-field intensity [A/m] |
| $H_m$ | Magnetic-field intensity from permanent magnet [A/m] |
| $J$ | Current density [$A/m^2$] |
| $J_t$ | Total current density [$A/m^2$] |
| $K_B$ | Total bend coefficient |
| $K_I$ | Bend resistance coefficient |
| $L$ | Total length of the pump duct [m] |
| $\mathcal{M}$ | Magnetisation [A/m] |

| | |
|---|---|
| $n$ | Number of pump duct turns [A/m] |
| $p$ | Developed pressure of the pump duct [Pa] |
| $p_h$ | Hydraulic pressure loss in the pump [Pa] |
| $r$ | Radius of pump duct [m] |
| $Re$ | Reynolds number |
| $t$ | Time [s] |
| $v$ | Velocity of fluid [m/s] |
| $\varepsilon_0$ | Permittivity in vacuum [F/m] |
| $\varepsilon_s$ | Roughness height [m] |
| $\mu_0$ | Permeability in vacuum [H/m] |
| $\mu_r$ | Relative permeability |
| $\nu$ | Kinematic viscosity [$m^2/s$] |
| $\rho$ | Density of the liquid metal [$kg/m^3$] |
| $\sigma$ | Electrical conductivity of liquid metal [$1/(\Omega \cdot m)$] |
| $\chi_m$ | Magnetic susceptibility |

## I. Introduction

The prototype fourth generation (gen-IV) sodium-cooled fast reactor (PGSFR) has the advantage that it can operate at atmospheric pressure by using liquid metal as a coolant.[1] Liquid sodium with high thermal conductivity and high boiling point of 882.8 °C is used as a coolant because only slight deceleration occurs against fast neutrons. A decay-heat-removal system is needed to remove the total decay and sensible heat from the reactor coolant to ensure that the temperature limit of the reactor system is not exceeded. The PGSFR has an electric output of 150 MWe, and uses decay heat exchangers (DHXs), which are located in the cold pool. The specification of DHXs is set as 4 MWe considering 1% of the rated core thermal power. An active decay-heat-removal system (ADHRS) and passive decay-heat-removal circuit (PDRC) have been considered to reduce the decay heat while the heat is released to the atmosphere, as shown in Fig. 1.[2] The ADHRS process requires active sodium circulation; therefore, a magnetohydrodynamics (MHD) transportation system, which generates developed pressure in a loop system using high-electrical conductivity materials, as shown in Fig. 2, is adopted as ADHRS owing to its advantages of simple maintenance and safety aspects.[3,4] In particular, the helical-type MHD transportation system offers the advantage of minimising current to reduce the size of the power supply, which is the main disadvantage of the rectangular-type system.[5] The pressure is created by the Lorentz force, which represents the vector product of an $r$-direction magnetic field and $z$-direction current density. The main variables of the helical-type MHD transportation system are shown in Fig. 3. The inner diameter, silver brazing, and number of turns are affected by the current according to the ratio of the inner diameter to the thickness of the flow channel, where the latter is fixed at 1 mm. The silver brazing is directly affected by the current. When the number of turns is increased, the required current decreases corresponding to its geometry. The inner diameter and radius of the pump affects the magnetic-flux density because the magnetic-flux density is affected by the magnetic permeability of the materials. The velocity is affected by the inner diameter under a fixed flowrate.[6,7] The Lorentz force generated by the vector product of current density and magnetic flux density, electromotive force generated by the velocity and magnetic flux density of liquid sodium, and hydraulic pressure loss[8] due to frictional force of the fluid were considered to calculate the input current[9] of the helical-type MHD transportation system. Therefore, the pressure generated by the Lorentz force, pressure

loss by the electromotive force, and hydraulic pressure loss relative to the parameters are analysed to optimise the helical-type MHD transportation system.[10] The specifications of the MHD transportation system are determined by the system pressure loss and mass flowrate for heat transfer, and are set as follows: developed pressure of 10 kPa and flowrate of 0.005 $m^3/s$ under a temperature of 468.75 K.[11] The helical-type MHD transportation system as seen in Fig.1 could remove decay heat actively with relatively low input current compared to rectangular-type one, and the helical-type MHD transportation system was analysed to minimize input current.

## II. Analysis of the helical-type MHD transportation system

The schematic of the helical-type MHD transportation system shows four component types, as shown in Fig. 2: ferromagnet, permanent magnet, electrode stub, and pump duct. The Lorentz force was generated by the vector product of the current density from the electrode stub in the $z$ direction and by the magnetic-flux density from the permanent magnet and ferromagnet in the $r$ direction,[12–15] where the liquid sodium flowed in the $\theta$ direction. The magnetic-flux density was determined by Maxwell's equation of Ampere's law, Faraday's law, Gauss's law for magnetism, and Ohm's law, as expressed in Eqs. (1)–(4) using the finite element method (FEM) that considered the material properties.[16–19]

$$\text{Ampere's law: } \nabla \times \vec{\mathrm{B}} = \mu_0(\vec{J} + \varepsilon_0 \frac{\partial E}{\partial t}) \tag{1}$$

$$\text{Faraday's law: } \nabla \times \vec{\mathrm{E}} = -\frac{\partial \vec{\mathrm{B}}}{\partial \mathrm{t}} \tag{2}$$

$$\text{Gauss's law for magnetism: } \nabla \cdot \vec{\mathrm{B}} = 0 \tag{3}$$

$$\text{Ohm's law: } \vec{\mathrm{J}} = \sigma(\vec{\mathrm{E}} + \vec{\mathrm{v}} \times \vec{\mathrm{B}}) \tag{4}$$

The equations of the electric field, current density, magnetic-flux density, and velocity of a liquid sodium are expressed by Eqs. (5)–(10). The $\theta$ direction electric field was eliminated owing to the symmetry of the pump duct. The magnetic-flux density was divided into external magnetic-flux density from the permanent magnet and induced magnetic-flux density from the electrode stub. The external magnetic-flux density in the $\theta$ direction was eliminated owing to the symmetry of the permanent magnet and ferromagnetic material. The fluid velocity contained only a $\theta$-direction component because the pump duct was installed along the $\theta$ direction, and the $z$-direction component was negligible because the pump-duct circumference was much higher than its radius. In other words, the angle of the pump duct was almost equal to zero.

$$\vec{\mathrm{E}}_t(r,\theta,z) = E_r\hat{r} + E_z\hat{z} \tag{5}$$

$$\vec{J}_t(r,\theta,z) = J_r\hat{r} + J_\theta\hat{\theta} + J_z\hat{z} \tag{6}$$

$$\vec{B}_t(r,\theta,z) = \vec{B}_i(r,\theta,z) + \vec{B}_e(r,\theta,z) \tag{7}$$

$$\vec{B}_i(r,\theta,z) = B_{i,r}\hat{r} + B_{i,\theta}\hat{\theta} + B_{i,z}\hat{z} \tag{8}$$

$$\vec{B}_e(r,\theta,z) = B_{e,r}\hat{r} + B_{e,z}\hat{z} \tag{9}$$

$$\vec{v}(r,\theta,z) = v_\theta \hat{\theta} \tag{10}$$

Ampere's law, given in Eq. (1), is expressed as Eqs. (11)–(14) using the curl operator calculation in a cylindrical coordinate. The direction $\theta$ of the magnetised material, which contains the permanent magnet, was symmetric; the ferromagnetic material had a condition of symmetry, and current density in the flow channel within the $\theta$ direction was symmetric. Therefore, all the induced and external magnetic flux were symmetric with respect to the $\theta$ direction, and thus, the $\frac{\partial}{\partial\theta}$ term of the magnetic-flux density was ignored. The external magnetic-flux density was generated by rotating electrons where a microscopically small current circulated. Therefore, only the induced magnetic-flux density was considered to calculate Ampere's law. The electric field due to the direct current was constant as time progressed; thus, the rate of change in the electric-field term was zero.

$$\nabla \times \vec{\mathrm{B}}_\mathrm{i} = \mu_0 \vec{J}_t \tag{11}$$

$$\nabla \times \vec{\mathrm{B}}_\mathrm{i} = \frac{\partial \mathrm{B_{i,\theta}}}{\partial z}\hat{\mathrm{r}} + \left(\frac{\partial \mathrm{B_{i,r}}}{\partial z} - \frac{\partial \mathrm{B_{i,z}}}{\partial r}\right)\hat{\theta} + \frac{1}{r}\frac{\partial (r\mathrm{B_{i,\theta}})}{\partial r}\hat{\mathrm{z}} \tag{12}$$

$$\mu_0 \vec{J}_t = \mu_0 (J_r \hat{r} + J_\theta \hat{\theta} + J_z \hat{z}) \tag{13}$$

$$\frac{\partial \mathrm{B_{i,\theta}}}{\partial z} = \mu_0 J_r, \frac{\partial \mathrm{B_{i,r}}}{\partial z} - \frac{\partial \mathrm{B_{i,z}}}{\partial r} = \mu_0 J_\theta, \frac{1}{r}\frac{\partial (r\mathrm{B_{i,\theta}})}{\partial r} = \mu_0 J_z \tag{14}$$

In the same manner, Faraday's law in Eq. (2) is expressed as Eqs. (15)–(17). The magnetic-flux density was not a time-varying function because the helical-type MHD transportation system used a permanent magnet and direct current. The $\frac{\partial}{\partial\theta}$ component of the electric field was also ignored owing to the symmetry of the permanent magnet, ferromagnet, and current density in the flow channel.

$$\nabla \times \vec{\mathrm{E}}_\mathrm{t} = 0 \tag{15}$$

$$\nabla \times \vec{\mathrm{E}}_\mathrm{t} = \left(\frac{\partial \mathrm{E_r}}{\partial z} - \frac{\partial \mathrm{E_z}}{\partial r}\right)\hat{\theta} \tag{16}$$

$$\frac{\partial \mathrm{E_r}}{\partial z} - \frac{\partial \mathrm{E_z}}{\partial r} = 0 \tag{17}$$

Gauss's law for magnetism in Eq. (3) is expressed as Eqs. (18)–(22) using the divergence operator in a cylindrical coordinate. The divergence in the total magnetic-flux density was zero, and that of the external magnetic-flux density from the permanent magnet was zero. Therefore, the induced magnetic-flux density was zero. The $\frac{\partial}{\partial\theta}$ component of the electric field was ignored owing to the symmetry of the helical-type MHD transportation system.

$$\nabla \cdot \vec{\mathrm{B}}_\mathrm{t} = \nabla \cdot \vec{\mathrm{B}}_\mathrm{i} + \nabla \cdot \vec{\mathrm{B}}_\mathrm{e} = 0 \tag{18}$$

$$\nabla \cdot \vec{\mathrm{B}}_\mathrm{e} = 0 \tag{19}$$

$$\nabla \cdot \vec{\mathrm{B}}_\mathrm{i} = 0 \tag{20}$$

$$\nabla \cdot \vec{\mathrm{B}}_\mathrm{e} = \frac{1}{r}\frac{\partial (rB_{e,r})}{\partial r} + \frac{\partial B_{e,z}}{\partial z} = 0 \tag{21}$$

$$\nabla \cdot \vec{B}_i = \frac{1}{r}\frac{\partial(rB_{i,r})}{\partial r} + \frac{\partial B_{i,z}}{\partial z} = 0 \tag{22}$$

Ohm's law in Eq. (4) is expressed as Eqs. (23)–(26) using the vector product. The θ direction current density was zero because the electric field in the θ direction and the vector product of the velocity and magnetic-flux density in the θ direction were zero.

$$\vec{J}_t = \sigma(\vec{E}_t + \vec{v} \times \vec{B}_t) \tag{23}$$

$$\vec{J}_t = J_r\hat{r} + J_\theta\hat{\theta} + J_z\hat{z} \tag{24}$$

$$\sigma\left(\vec{E}_t + \vec{v} \times \vec{B}_t\right) = \sigma\left\{\left(E_r + v_\theta B_{i,z} + v_\theta B_{e,z}\right)\hat{r} + \left(E_z - v_\theta B_{i,r} - v_\theta B_{e,r}\right)\hat{z}\right\} \tag{25}$$

$$J_r = \sigma(E_r + v_\theta B_{i,z} + v_\theta B_{e,z}), J_\theta = 0, J_z = \sigma(E_z - v_\theta B_{i,r} - v_\theta B_{e,r}) \tag{26}$$

Therefore, the relationship between the electric field and magnetic-flux density was obtained by combining Eqs. (14) and (26), as expressed in Eqs. (27) and (28).

$$\frac{\partial B_{i,r}}{\partial z} = \frac{\partial B_{i,z}}{\partial r} \tag{27}$$

$$\frac{1}{\mu_0\sigma}\frac{\partial B_{i,\theta}}{\partial z} = E_r + v_\theta B_{i,z} + v_\theta B_{e,z}, \frac{1}{\mu_0\sigma}\frac{1}{r}\frac{\partial(rB_{i,\theta})}{\partial r} = E_z - v_\theta B_{i,r} - v_\theta B_{e,r} \tag{28}$$

The electric field was eliminated using Eq. (17); therefore, the magnetic-flux density relationship is expressed in Eq. (29).

$$\frac{1}{\mu_0\sigma}\left\{\frac{\partial^2 B_{i,\theta}}{\partial z^2} - \frac{1}{r}\frac{\partial^2(rB_{i,\theta})}{\partial r^2} + \frac{1}{r^2}\frac{\partial(rB_{i,\theta})}{dr}\right\} = v_\theta(B_{i,z} + v_\theta B_{e,z} + v_\theta B_{i,r} + v_\theta B_{e,r}) \tag{29}$$

The magnetic-flux density in the flow channel was analysed by applying the magnetic coercivity of the permanent magnet ($Sm_2Co_{17}$) and magnetic permeability of the ferromagnet (1010 steel) using FEM. The magnetisation can be expressed as Eq. (30) by considering the permanent magnet and ferromagnet.

$$\vec{M} = \chi_m\vec{H} + \vec{H}_m \tag{30}$$

The total magnetic-flux density in the helical-type MHD transportation system was calculated using Eq. (31) by considering the permanent magnetic field ($H_m$) and independent local magnetic field.

$$\vec{B} = \mu_0\left(\vec{H} + \vec{M}\right) = \mu_0\mu_r\vec{H} + \mu_0\vec{H}_m \tag{31}$$

The boundary conditions of the magnetic-flux density and magnetic-field intensity between the different magnetic permeability materials were applied using Eqs. (32)-(34).

$$\vec{H}_{t,1} = \vec{H}_{t,2} \tag{32}$$

$$\vec{B}_{n,1} = \vec{B}_{n,2} \tag{33}$$

$$\vec{H}_t\big|_{r=\infty} = 0 \tag{34}$$

The tangential component of the magnetic-field intensity and normal component of the magnetic-flux density between high- (1010 steel) and low-magnetic permeability materials (air, stainless steel 316L, C103, and $Sm_2Co_{17}$) at the interface were applied to solve the

magnetic-flux density and flux line in the helical-type MHD transportation system using the ANSYS electromagnetic code simulation.

The helical-type MHD transportation system requires the Lorentz force to generate the velocity of the fluid in the narrow channel, as expressed in Eq. (35). The θ-direction Lorentz force only affected the velocity of the fluid in Eq. (10), and it is expressed in Eq. (36).

$$\begin{aligned}\vec{\mathrm{f}} = \vec{\mathrm{J}} \times \vec{\mathrm{B}} = &\left\{\sigma E_\theta\left(B_{i,r} + B_{e,r}\right) - \sigma\left(v_\theta B_{i,z} - v_\theta B_{e,z}\right)\left(B_{i,\theta} + B_{e,\theta}\right)\right\}\hat{\mathrm{z}} \\ &+\left\{\sigma\left(E_z + v_\theta B_{i,r} + v_y B_{e,r}\right)\left(B_{i,r} + B_{e,r}\right) - \sigma\left(v_\theta B_{i,z} + v_y B_{e,z}\right)\left(B_{i,z} + B_{e,z}\right)\right\}\hat{\theta} \\ &+\left\{\sigma\left(E_z + v_\theta B_{i,r} + v_\theta B_{e,r}\right)\left(B_{i,\theta} + B_{e,\theta}\right) - \sigma E_\theta\left(B_{i,z} + B_{e,z}\right)\right\}\hat{\mathrm{r}} \end{aligned} \quad (35)$$

$$\mathrm{f}_\theta = \sigma\left(E_z + v_\theta B_{i,r} + v_\theta B_{e,r}\right)\left(B_{i,r} + B_{e,r}\right) \quad (36)$$

The vector product of the current density in the $z$ direction and magnetic-flux density in the $r$ direction could be ignored as opposed to the current density in the $r$ direction and magnetic-flux density in the $z$ direction according to Eqs. (26) and (36). The electric field in the $r$ direction could be ignored as opposed to the electric field in the $z$ direction because current flowed along the $z$ direction, and the gap in the pump duct was narrow. The induced magnetic-flux density in the $r$ and $z$ directions could be ignored because the electric field in the $r$ direction was negligible. The external magnetic-flux density in the $z$ direction in the flow channel was negligible compared with that in the $r$ direction because the ferromagnetic material induced a magnetic flux along the $r$ direction. The $r$ direction magnetic flux density was dominantly influenced by the Lorentz force. The Lorentz force obtained from Eq. (35) was applied below as MHD equations.

The Navier–Stokes equation for MHD is expressed using Eq. (37), which can be reduced to Eq. (38) for steady-state incompressible flow of liquid sodium, where the viscosity term was ignored in the MHD transportation system with the high Hartmann number owing to the magnetic field[20]. Therefore, the pressure gradient in the Navier–Stokes equation can be expressed as the current density multiplied by the magnetic-flux density.

$$\rho\left(\frac{\partial}{\partial t} + v \cdot \nabla\right) v = -\nabla p + \rho v \nabla^2 v + \vec{J}_t \times \vec{B} \quad (37)$$

$$\nabla p = \vec{J}_t \times \vec{B} \quad (38)$$

The hydraulic pressure loss between the flow inlet and outlet, $\Delta p_h$, was calculated using the Darcy–Weisbach formula in Eq. (39), where the Darcy friction coefficient of turbulent flow, $f_d$, from the Colebrook–White equation[21] is given in Eq. (40), and total bend coefficient of $K_B$ is given in Eq. (41)[22].

$$\Delta \mathrm{p_h} = \mathrm{f_d}\rho \mathrm{L} v_\theta^2 / 2\mathrm{D} + \mathrm{K_B}\rho \mathrm{L} v_\theta^2 / 2, \quad (39)$$

$$\frac{1}{\sqrt{\mathrm{f_d}}} = -1.8 \log_{10}\left[\frac{6.9}{\mathrm{Re}} + \left(\frac{\varepsilon_\mathrm{s}}{3.7\mathrm{D}}\right)^{1.11}\right] \quad (40)$$

$$\mathrm{K_B} = (n-1)(0.25\pi f_r r/d + 0.5K_1) + K_1 \quad (41)$$

Combining Eqs. (35)–(41) yields the developed pressure between the flow inlet and outlet considering hydraulic pressure, as expressed in Eq. (42).

$$\Delta p = 4\int\{\sigma(E_z + v_\theta B_{i,r} + v_\theta B_{e,r})(B_{i,r} + B_{e,r})\}dV/\pi d^2 - f_d \rho L v_\theta^2/2D - K_B \rho L v_\theta^2/2 \quad (42)$$

The FEM was implemented using ANSYS electromagnetic suite version 17.1 for the calculation of magnetic-flux density and current density, and the total developed pressure was calculated using Eq. (42). The input current was supplied under 10 kPa of developed pressure at a flowrate of 0.005 $m^3/s$ based on the calculated result of developed pressure, which is the combined result of both the FEM and Eq. (42).

## III. Results and Discussion

The helical-type MHD transportation system was analysed in terms of the current, magnetic-flux density, and pressure. The optimisation consisted of the required pump current, which is the main limitation of a helical-type MHD transportation system that determines its efficiency. In other words, the developed pressure was optimised because it directly affects the current when determining the developed pressure. To optimise the developed pressure, the current and magnetic-flux density should be calculated for this geometry. These parameters were numerically analysed using the FEM in the ANSYS simulation.

### *3.1. Current*

The current was affected by the helical-type MHD transportation system geometry because the material components of the pump exhibited different electrical conductivities. The main parameters being analysed were the inner and outer diameters of the flow channel and the silver brazing. In particular, the thickness of the flow channel was fixed at 0.001 m as the minimum because it disturbs the current flow in sodium while enduring its physical pressure. The tendency of the silver brazing when the inner diameter of the flow channel was 0.06 mm is shown in Fig. 4. The current ratio of sodium to the total components decreased as the ratio of the silver-brazing size to the outer diameter of the flow channel was increased because the electric conductivity of silver is much higher than that of sodium and the flow channel (stainless steel 316 L). The current was fringed to the silver when the silver-brazing ratio increased. Therefore, the size of the silver brazing was determined to be less than 6% compared with the outer diameter of the flow channel whose value was 99% of the current ratio. The inner diameter was affected by the current ratio because current could flow in the flow channel, as shown in Fig. 5. More current flowed in sodium as the inner diameter was increased considering its linear current path, and the current ratio was almost constant when the inner diameter of the flow channel was more than 0.03 m because the flow channel did not disturb the current flowing in sodium with a flat geometry. This result was considered when the pressure generated by the Lorentz force was calculated.

### *3.2. Magnetic-flux density*

The variables that affected the magnetic-flux density of the helical-type MHD transportation system were the inner diameter of the flow channel, radius of the pump, and ferromagnet thickness. The developed pressure increased as the magnetic-flux density increased in this helical-type MHD transportation system structure. Therefore, the ferromagnet thickness was maximised to infinity when it was analysed. The width of the flow channel was determined by adding 6 mm to the inner diameter of the flow channel considering the heat coil and insulator. The inner radius affected the magnetic-flux density

because the relative magnetic permeability of the materials was one except for the ferromagnet. When the inner radius was increased, the *r*-direction magnetic-flux density decreased due to the decreasing region of high magnetic permeability, as shown in Fig. 6. The pump radius affected the magnetic-flux density in the flow channel. The tendency of the magnetic-flux density showed an increase when the pump radius was increased because of the high permeability of the inner ferromagnet. However, when the radius of the pump was larger than 0.16 m, the magnetic-flux density decreased when the radius of the pump was increased because the repulsive force among the permanent magnets was reduced, as shown in Fig. 6. The height of the pump-duct region was fixed at 0.5 m considering the space problem and maintenance of the helical-type MHD transportation system. The tendency of the magnetic-flux density at the middle of the flow-channel width is shown in Fig. 7. The *r*-direction magnetic-flux density was maximum at the middle, and it rapidly decreased at the end part because the flux line shifted to the *z* direction moving to the end part. The flow channel was installed at 0.3 m of the flow-channel height to maximise the magnetic-flux density of sodium. The outer ferromagnet height and thickness were determined to be maximum while the size and weight of the pump was minimised, as shown in Figs. 8 and 9, with values of 0.08 and 0.06 m, respectively, at a magnetic-flux density of 0.466 T; this is because the magnetic-flux density affected the developed pressure, as shown in Fig. 10. The developed pressure increased as the magnetic-flux density due to the Lorentz force proportionally increased, whereas the pressure loss was less than the developed pressure below a magnetic flux density of 0.16 T. The magnetic-flux density result was considered to solve the problem of the pressure generated by the Lorentz force and pressure loss caused by the electromotive force.

### *3.3. Pressure*

The pressure was divided into three parts, namely, the pressure generated by the Lorentz force, pressure loss caused by the electromotive force, and hydraulic pressure loss. The number of turns was the dominant factor that determined the developed pressure because it determined the force generated at each pump-duct turn. The pressure due to the number of turns is shown in Fig. 11, which was proportional to all other pressures and determined by the height of the flow channel divided by the outer diameter of the flow channel, rounded to the nearest integer. The pressure generated by the Lorentz force is shown in Fig. 12 as a 3D plot and as 2D log-scale plots at a 352 A input current. The number of turns contributed to the developed pressure, and the pressure was maximum at 0.3 m of the flow-channel height. The pressure generated by the Lorentz force decreased as the inner diameter of the flow channel increased. The main reason for the decrease was that as the inner diameter was reduced, the pressure became inversely proportional to the flow-channel area. The current ratio shown in Fig. 5 and magnetic-flux density shown in Fig. 6 also contributed to the pressure generated by the Lorentz force. The pressure loss due to electromotive force is shown in Fig. 13, considering the inner diameter of the flow channel and pump radius. The tendency was determined by the square of the magnetic-flux density (Fig. 6) and velocity, which was inversely proportional to the flow-channel area. The hydraulic pressure loss which is proportional to velocity squared is shown in Fig. 14. Therefore, the hydraulic pressure showed a rapid decrease when the inner diameter of the flow channel was increased. The pump radius affected the hydraulic pressure loss because it increased the total length of the pump duct, causing friction between sodium and the flow channel. The developed pressure, which was equal to the pressure generated by the Lorentz force minus the pressure losses, is shown in Fig. 15, which shows a zero value below a 0.045 m inner diameter; this because the pressure loss was higher than the developed pressure generated by the Lorentz force. The

maximum pressure was 10 kPa when the inner diameter of the flow channel was equal to 0.06 m and the pump radius was equal to 0.16 m. In conclusion, the required current was minimised at the same specification of the maximum developed pressure obtained at 352 A, as shown in Fig. 16 and the design specifications listed in Table 1. The result could be reliable because the simulation using the commercial ANSYS electromagnetic suite version 17.1 simulation was also performed for another type of MHD transportation device described in Kwak's thesis.[23] The electromagnetic characteristics of the flow channel in the helical-type MHD are plotted in Fig. 17. This current value is only 6.2% of the required current compared with 5671 A of a rectangular-type MHD transportation system[11], given in Table 2 under the same condition that leads to a decrease in the power-supply-cost problem.[24] The pressure–flowrate curve shown in Fig. 18 displays a negative slope, which indicates the negative feedback action between the pressure and flow in sodium. This could stabilize the flow of fluid sodium in the flow channel and ensure the sufficient cooling capacity of an ADHRS in a Gen-IV reactor.

## IV. Conclusion

The numerical optimisation of a helical-type MHD transportation system for the liquid-metal-cooling-type PGSFR with high uranium utilisation was performed in terms of the inner diameter of the flow channel, silver-brazing size, number of turns, ferromagnet thickness, and pump radius. The generated pressure by the Lorentz force and pressure loss caused by the electromotive force and hydraulic friction was considered to calculate the developed pressure and input current. The inner diameter of the flow channel and pump radius with values of 0.06 and 0.16 m, respectively, were analysed relative to the pressure and current for the optimize input current of a helical-type MHD transportation system. The optimum input current was shown to be much less than that of a rectangular-type MHD transportation system, 352 A at the developed pressure of 10 kPa and the flowrate of 0.005 $m^3/s$ under an operating temperature of 468.75 K. Therefore, the helical-type MHD transportation system was considered effective for use in the ADHRS of a PGSFR to increase cooling capacity.

**References**

1. Lopez-Solis, R., François, J. L. The breed and burn nuclear reactor: A chronological, conceptual, and technological review. Int J Energy Res 2017; 43(3): 953-965.

2. Lee HY, Eoh JH, Lee YB. High temperature design of finned-tube sodium-to air heat exchanger in a sodium test loop. Nucl Eng Des 2013; 265: 833-840.

3. Baker RS, Tessier MJ. Handbook of electromagnetic pump technology. New York: Elsevier; 1987.

4. Blake LR. Conduction and induction pumps for liquid metals. Proc IEE-Part A: Power Engineering. 1957; 104(13): 49-67.

5. Lee GH, Kim HR. The numerical investigation and comparison of the rectangular, cylindrical and helical type DC electromagnetic pump. 10th PAMIR International Conference. Italy 2016.

6. Babic SI, Akyel C. Improvement in the analytical calculation of the magnetic field produced by permanent magnet rings. Prog Electromagn Res C 2008; 5: 71-82.

7. Gutierrez AU, Heckathorn CE. Electromagnetic pumps for liquid metals. Naval Postgraduate School, California 1965.

8. Bennecib N, Drid S, Abdessemed R. Numerical investigation of flow in a new DC pump MHD. J Appl Fluid Mech 2009; 2(2): 23-28.

9. Nashine BK, Dash SK, Gurumurthy K, Rajan M, Vaidyanathan G. Design and testing of DC conduction pump for sodium cooled fast reactor. In 14th International Conference on Nuclear Engineering, American Society of Mechanical Engineers 2006.

10. Nashine BK, Dash SK, Gurumurthy K. Kale U, Sharma IV VD, Prabhaker R, Rajan M. Vaidyanathan G. Performance testing of indigenously developed DC conduction pump for sodium cooled fast reactor. Indian J Eng Mater Sci 2007;14: 209-214.

11. Kim D, Hong J, Lee T. Design of DC conduction pump for PGSFR active decay heat removal system. Transactions of the Korean Nuclear Society Spring Meeting, Korea 2014.

12. Moffatt HK. Field generation in electrically conducting fluids. Cambridge University Press, New York 1978.

13. Zhu ZQ, Howe D. Analytical prediction of the cogging torque in radial-field permanent magnet brushless motors. IEEE Trans Magn 1992; 28(2): 1371-1374.

14. Oka T, Kawasaki N, Fukui S. Ogawa J, Sato T, Terasawa T, Itoh Y, Yabuno R. Magnetic field distribution of permanent magnet magnetized by static magnetic field generated by HTS bulk magnet. IEEE Trans Appl Supercond 2012; 22(3).

15. Kikuchi S, Murakami K. Behavior of a new DC electromagnetic pump using superconducting magnet. IEEE Trans Magn 1977; 13(5): 1559-1561.

16. Sobolev V. Database of thermophysical properties of liquid metal coolants for GEN-

IV. SCK• CEN. Mol, Belgium 2011.

17. Ohse RW. Handbook of thermodynamic and transport properties of alkali metals. Oxford 1985.

18. Ho CY, Chu TK. Electrical resistivity and thermal conductivity of nine selected AISI stainless steels. CINDAS Report 45, Washington 1977.

19. Hughes M, Pericleous KA, Cross M. The numerical modelling of DC electromagnetic pump and brake flow. Appl Math Model 1995; 19(12): 713-723.

20. Tillack MS, Morley NB. Magnetohydrodynamics. Standard Handbook for Electrical Engineers 1998.

21. Haaland SE. Simple and explicit formulas for the friction factor in turbulent pipe flow. J Fluids Eng 1983; 105: 89-90.

22. Crane. Flow of fluids: through valves, fittings, and pipe. 1977.

23. Kwak J, Kim, HR. Magnetic field analysis of an electromagnetic pump for sodium thermohydraulic test in the Sodium Test Loop for Safety Simulation and Assessment—Phase 1. Prog Nucl Energy 2017; 101: 235-242.

24. Lee GH, Kim, HR. Numerical investigation and comparison of the rectangular, cylindrical, and helical-type dc electromagnetic pumps. Magnetohydrodynamics 2017; 53(2): 429-438.

**Figure captions**

**Table captions**

Table 1 Design specifications of the helical-type MHD transportation system from the analytical solution.

Table 2 Comparison of the design specifications between helical-type MHD transportation system and rectangular-type MHD transportation system.

Table 1

| | Variables | Unit | Values |
|---|---|---|---|
| Hydrodynamic | Flow rate | $[m^3/s]$ | 0.005 |
| | Developed pressure | [kPa] | 10 |
| | Temperature | [K] | 468.75 |
| | Velocity | [m/s] | 1.5 |
| | Reynolds number | | 282300 |
| | Pressure generated by Lorentz force | [kPa] | 17.2 |
| | Pressure loss by the electromotive force | [kPa] | 5.5 |
| | Hydraulic pressure loss | [kPa] | 1.7 |
| Geometrical | Inner diameter of the flow channel | [m] | 0.06 |
| | Thickness of the flow channel | [m] | 0.001 |
| | Ferromagnet height | [m] | 0.08 |
| | Ferromagnet thickness | [m] | 0.06 |
| | Radius of pump | [m] | 0.16 |
| | Number of turns | | 5 |
| Electrical | Input current | [A] | 352 |
| | Magnetic-flux density | [T] | 0.466 |

Table 2

| Variables | Unit | Values (Helical-type) | Values (Rectangular-type) |
|---|---|---|---|
| Flow rate | $[m^3/s]$ | 0.005 | |
| Developed pressure | [kPa] | 10 | |
| Temperature | [K] | 468.75 | |
| Velocity | [m/s] | 1.5 | 2.7 |
| Hydraulic pressure loss | [kPa] | 1.7 | 4.3 |
| Magnetic-flux density | [T] | 0.466 | 0.134 |
| Input current | [A] | 352 | 5671 |

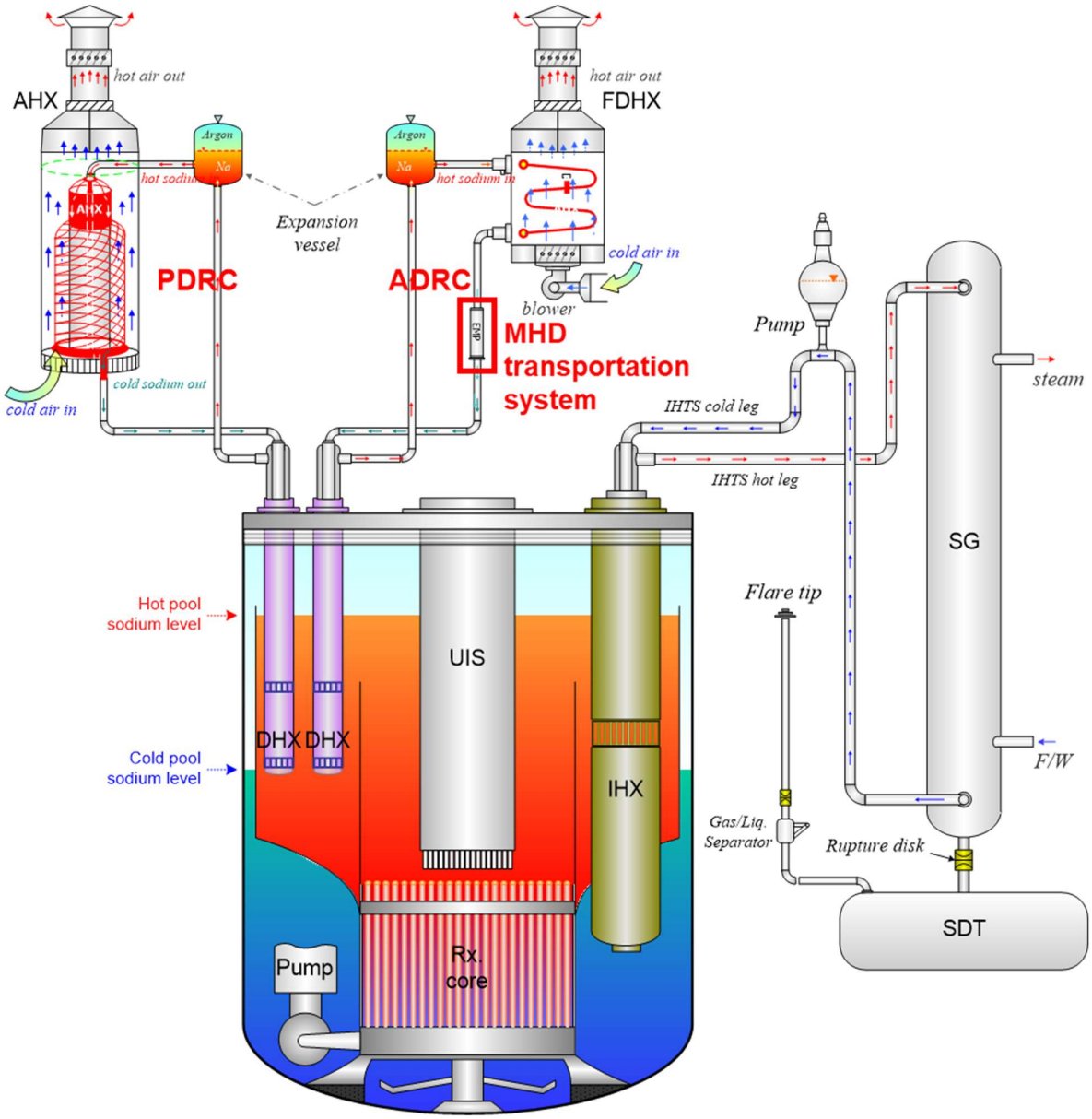
AHX
hot air out
Argon
Na
hot sodium
Expansion vessel
hot sodium in
FDHX
hot air out
cold air in
blower
PDRC
ADRC
EMP
MHD transportation system
cold sodium out
cold air in
Pump
steam
IHTS cold leg
IHTS hot leg
SG
Flare tip
Hot pool sodium level
UIS
DHX DHX
Cold pool sodium level
IHX
F/W
Gas/Liq. Separator
Rupture disk
SDT
Pump
Rx. core

Fig. 1

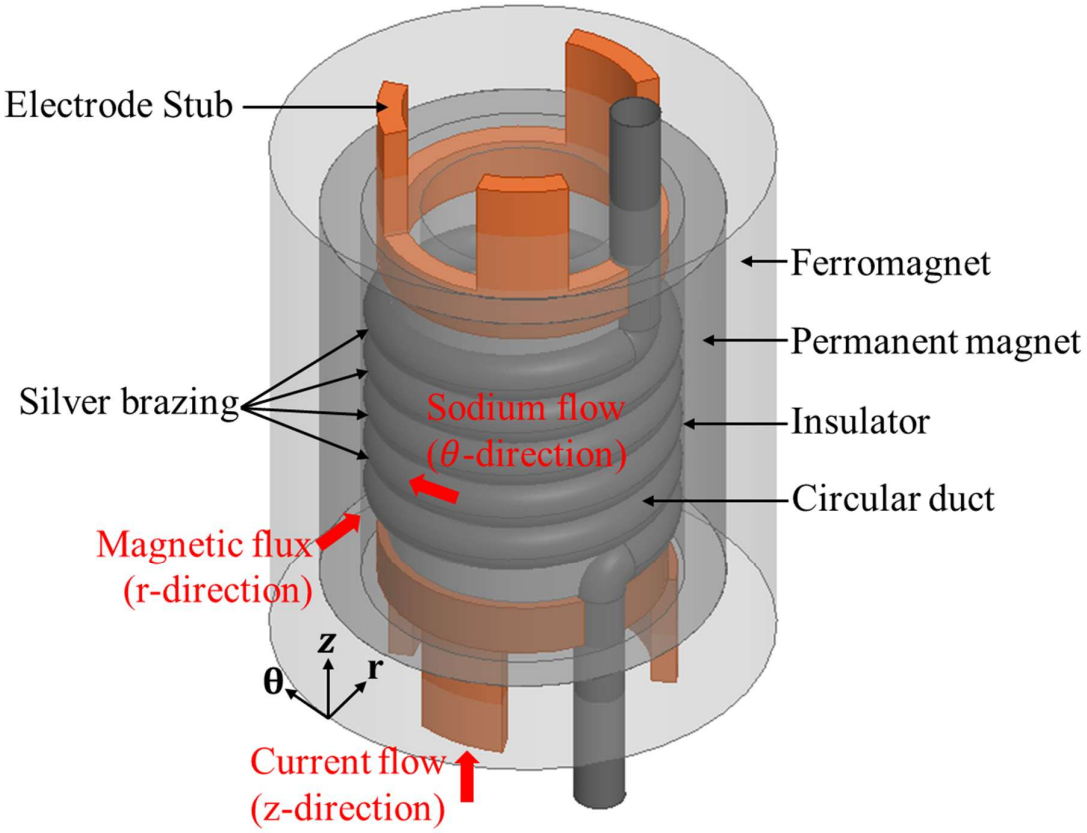
Electrode Stub
Ferromagnet
Permanent magnet
Silver brazing
Sodium flow
(θ-direction)
Insulator
Circular duct
Magnetic flux
(r-direction)
z
r
θ
Current flow
(z-direction)

Fig. 2

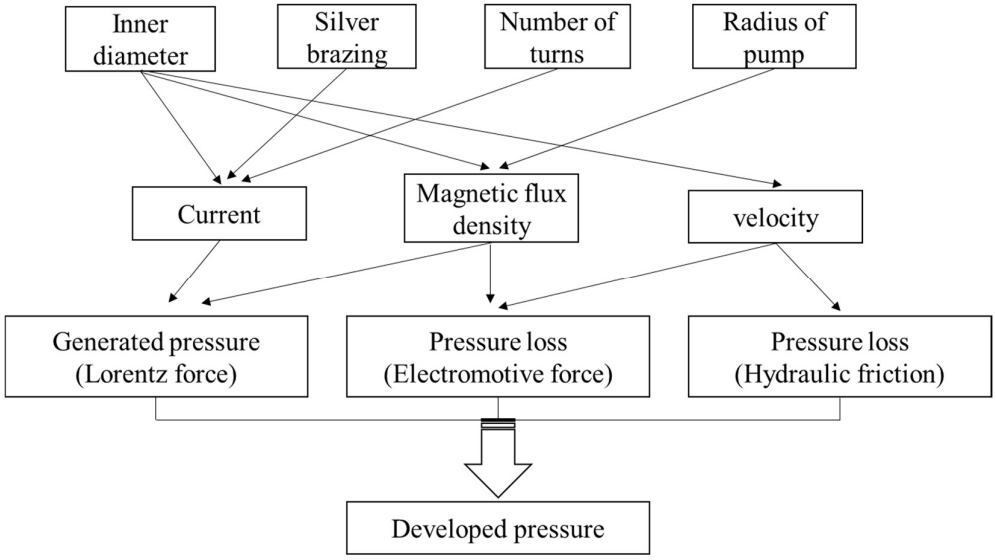
Inner diameter
Silver brazing
Number of turns
Radius of pump
Current
Magnetic flux density
velocity
Generated pressure (Lorentz force)
Pressure loss (Electromotive force)
Pressure loss (Hydraulic friction)
Developed pressure

Fig. 3

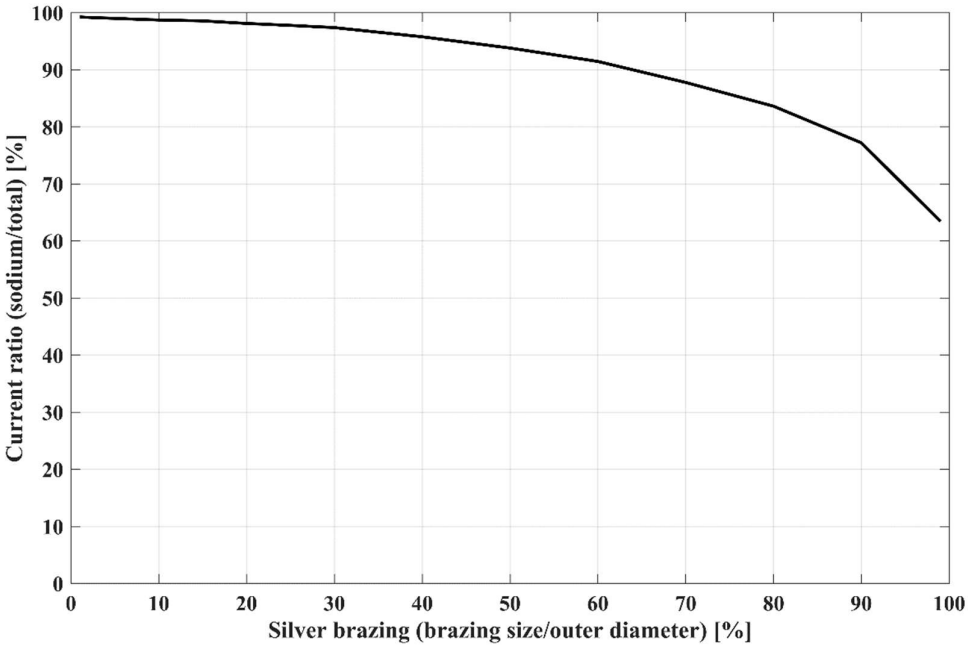
Current ratio (sodium/total) [%]
Silver brazing (brazing size/outer diameter) [%]
0
10
20
30
40
50
60
70
80
90
100

Fig. 4

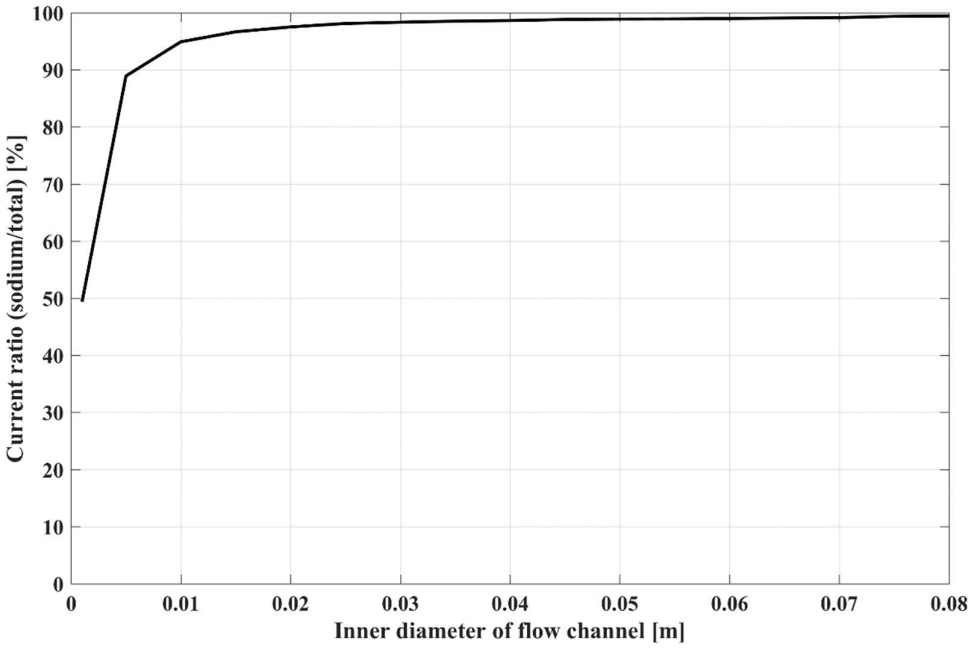
Current ratio (sodium/total) [%]
Inner diameter of flow channel [m]
0
10
20
30
40
50
60
70
80
90
100
0.01
0.02
0.03
0.04
0.05
0.06
0.07
0.08

Fig. 5

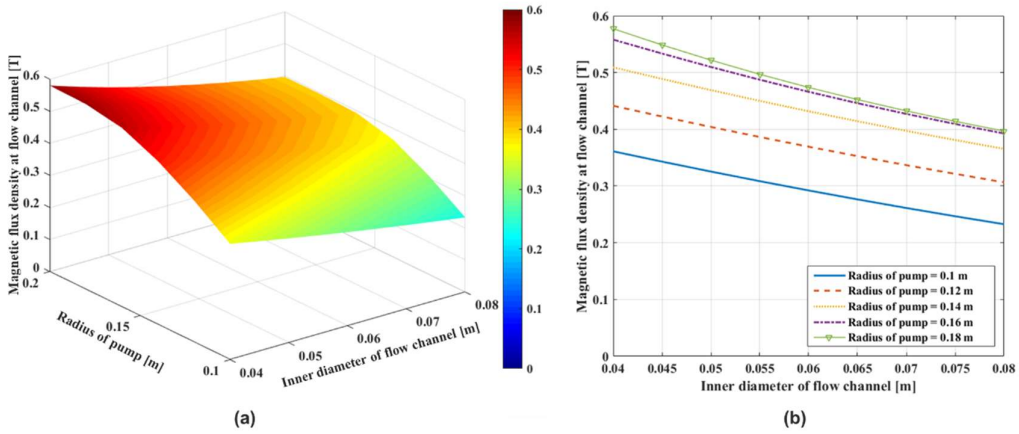
Magnetic flux density at flow channel [T]
Radius of pump [m]
Inner diameter of flow channel [m]
(a)
Magnetic flux density at flow channel [T]
Inner diameter of flow channel [m]
Radius of pump = 0.1 m
Radius of pump = 0.12 m
Radius of pump = 0.14 m
Radius of pump = 0.16 m
Radius of pump = 0.18 m
(b)

Fig. 6

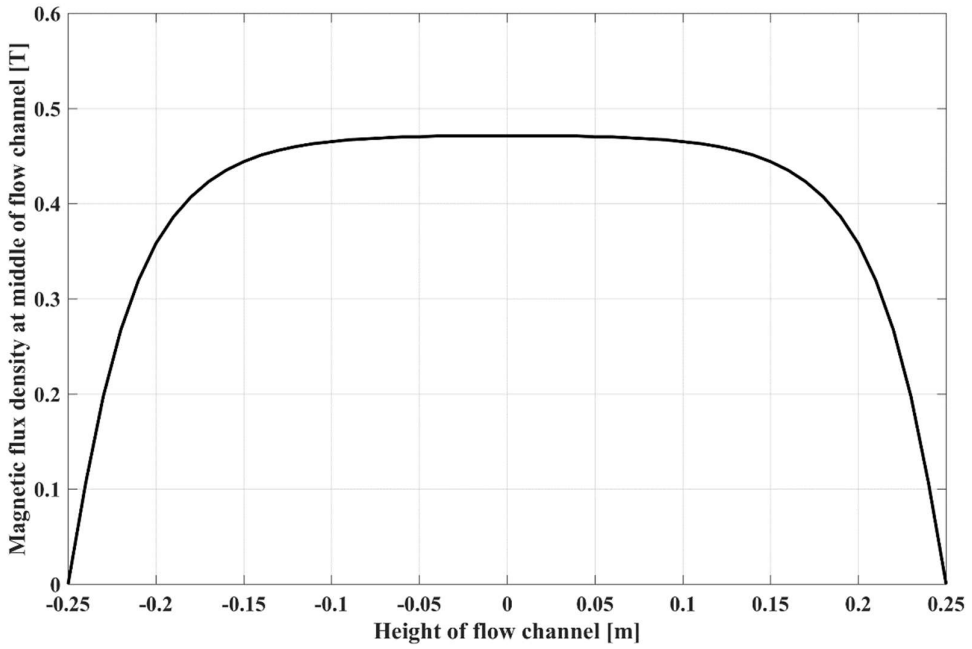
Magnetic flux density at middle of flow channel [T]
Height of flow channel [m]

Fig. 7

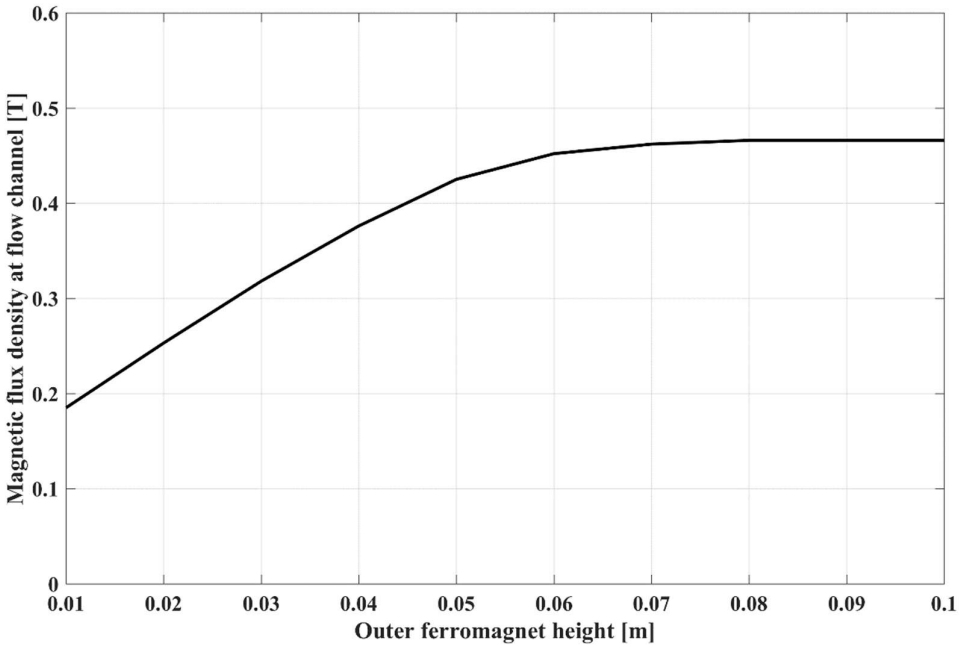
Magnetic flux density at flow channel [T]
0.6
0.5
0.4
0.3
0.2
0.1
0
0.01
0.02
0.03
0.04
0.05
0.06
0.07
0.08
0.09
0.1
Outer ferromagnet height [m]

Fig. 8

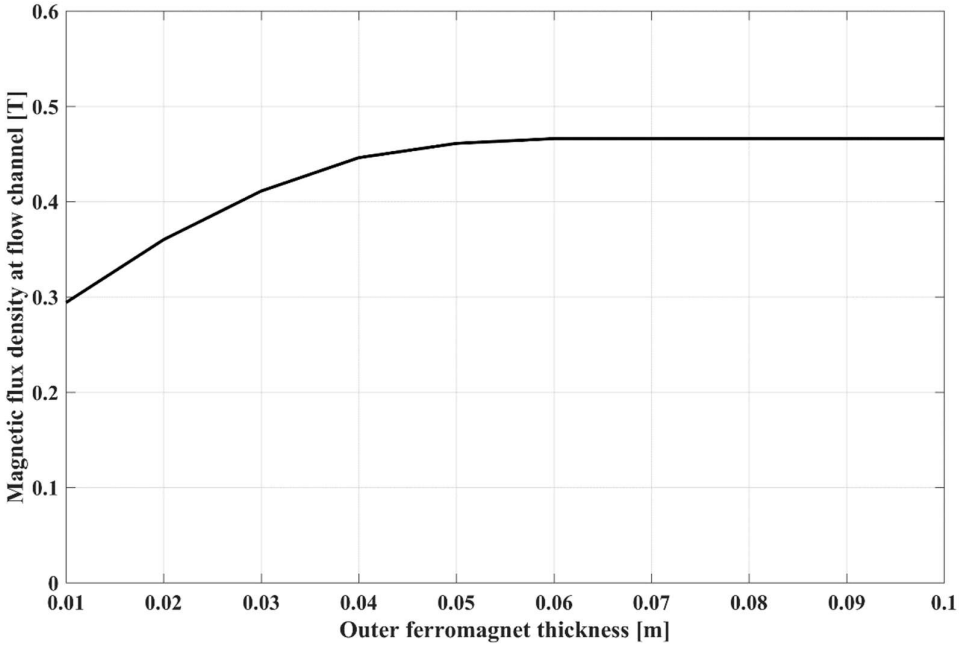
Magnetic flux density at flow channel [T]
0.6
0.5
0.4
0.3
0.2
0.1
0
0.01
0.02
0.03
0.04
0.05
0.06
0.07
0.08
0.09
0.1
Outer ferromagnet thickness [m]

Fig. 9

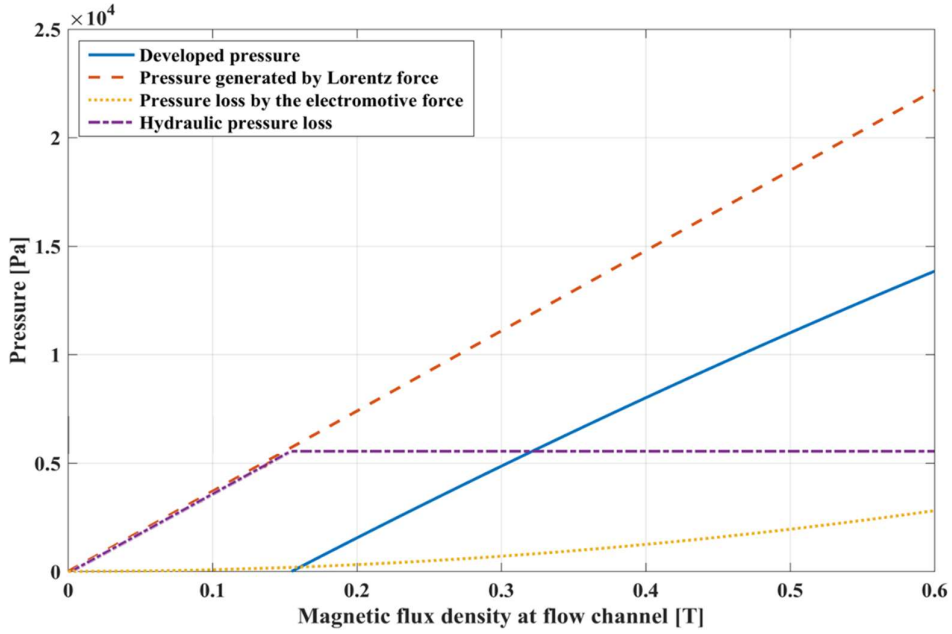
×10^4
2.5
2
1.5
1
0.5
0
Pressure [Pa]
Developed pressure
Pressure generated by Lorentz force
Pressure loss by the electromotive force
Hydraulic pressure loss
0
0.1
0.2
0.3
0.4
0.5
0.6
Magnetic flux density at flow channel [T]

Fig. 10

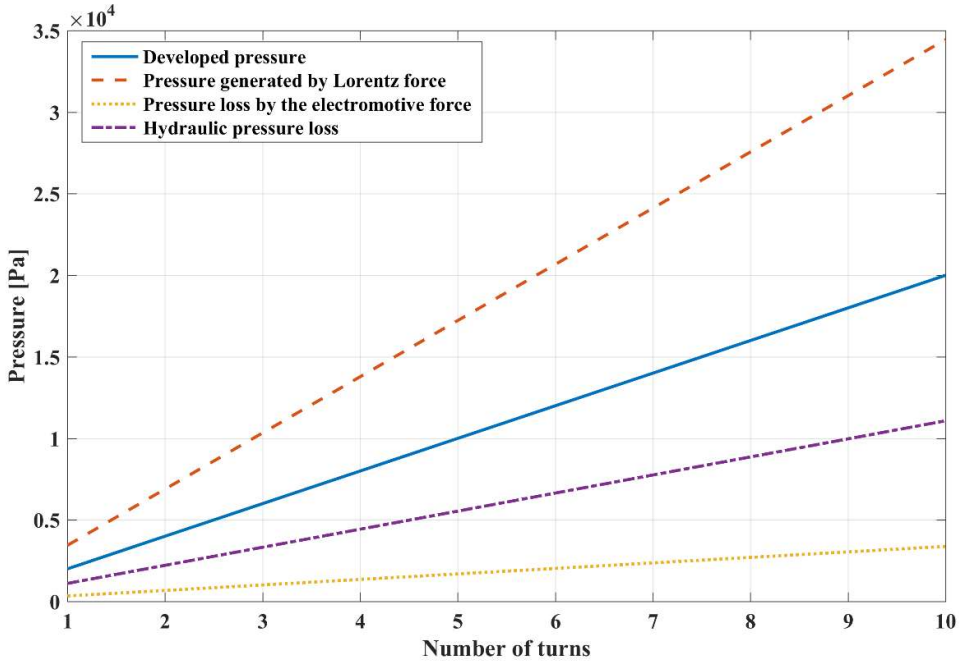
×10^4
3.5
3
2.5
2
1.5
1
0.5
0
Pressure [Pa]
Developed pressure
Pressure generated by Lorentz force
Pressure loss by the electromotive force
Hydraulic pressure loss
1
2
3
4
5
6
7
8
9
10
Number of turns

Fig. 11

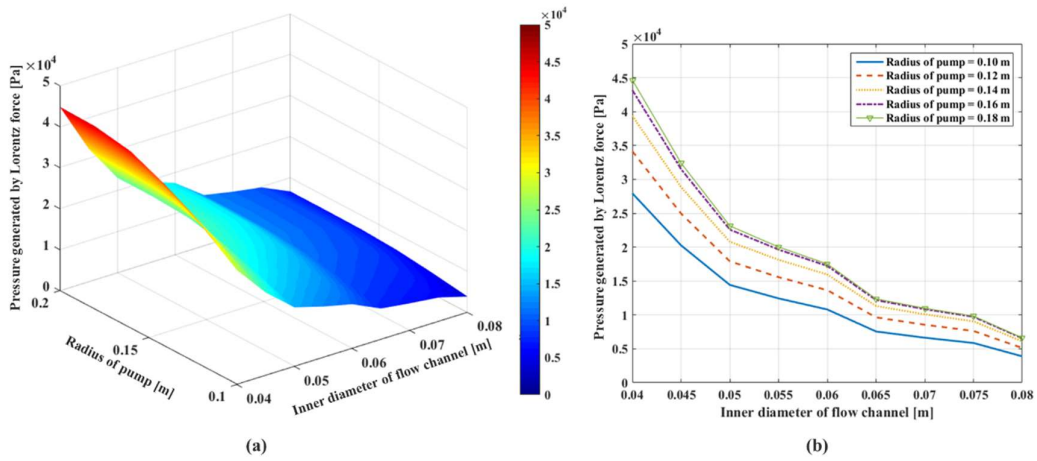
Pressure generated by Lorentz force [Pa]
×10^4
Radius of pump [m]
Inner diameter of flow channel [m]
Radius of pump = 0.10 m
Radius of pump = 0.12 m
Radius of pump = 0.14 m
Radius of pump = 0.16 m
Radius of pump = 0.18 m
Inner diameter of flow channel [m]
(a)
(b)

Fig. 12

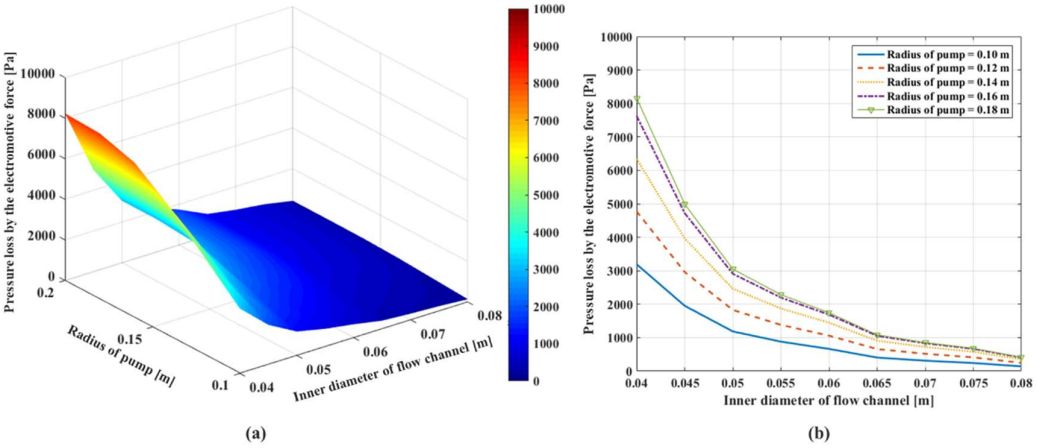
Pressure loss by the electromotive force [Pa]
Radius of pump [m]
Inner diameter of flow channel [m]
Radius of pump = 0.10 m
Radius of pump = 0.12 m
Radius of pump = 0.14 m
Radius of pump = 0.16 m
Radius of pump = 0.18 m
Inner diameter of flow channel [m]
(a)
(b)

Fig. 13

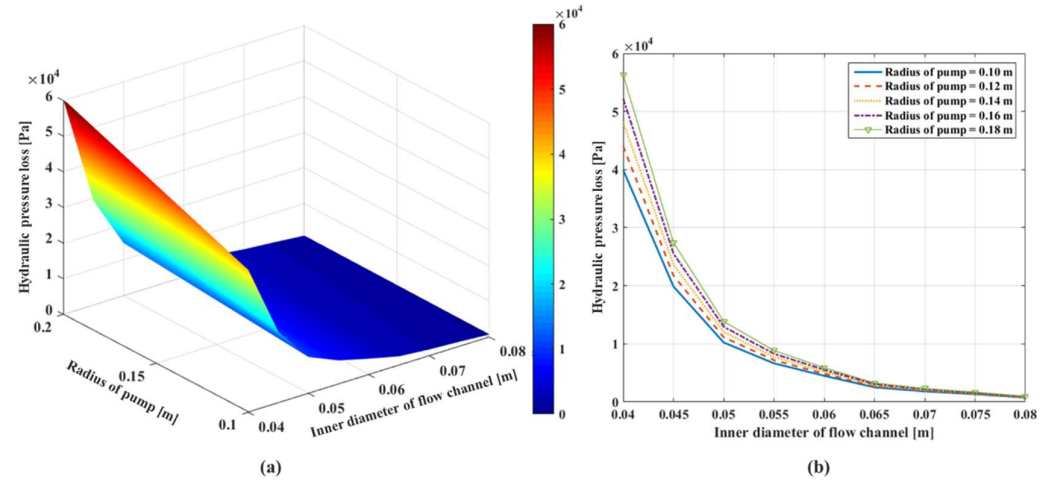
Hydraulic pressure loss [Pa]
×10^4
Radius of pump [m]
Inner diameter of flow channel [m]
Radius of pump = 0.10 m
Radius of pump = 0.12 m
Radius of pump = 0.14 m
Radius of pump = 0.16 m
Radius of pump = 0.18 m
Inner diameter of flow channel [m]
(a)
(b)

Fig. 14

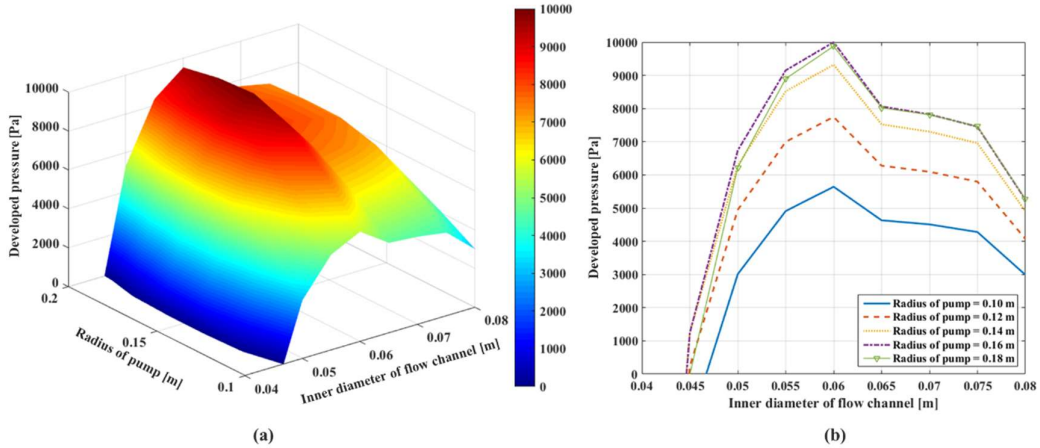


Fig. 15

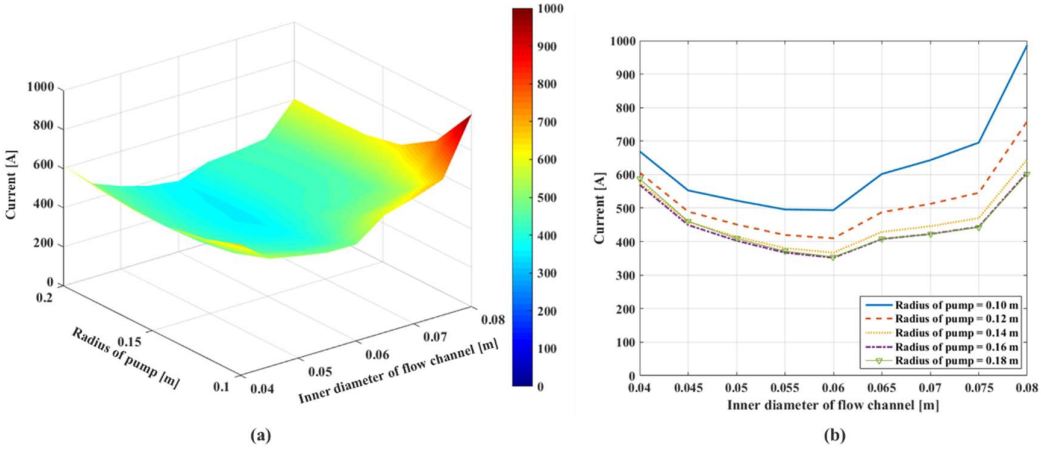


Fig. 16

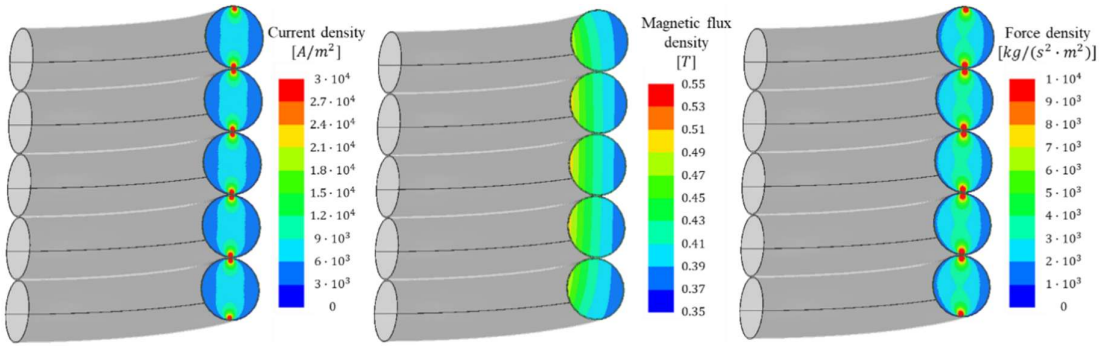
Current density
$[A/m^2]$
$3 \cdot 10^4$
$2.7 \cdot 10^4$
$2.4 \cdot 10^4$
$2.1 \cdot 10^4$
$1.8 \cdot 10^4$
$1.5 \cdot 10^4$
$1.2 \cdot 10^4$
$9 \cdot 10^3$
$6 \cdot 10^3$
$3 \cdot 10^3$
0
Magnetic flux density
$[T]$
0.55
0.53
0.51
0.49
0.47
0.45
0.43
0.41
0.39
0.37
0.35
Force density
$[kg/(s^2 \cdot m^2)]$
$1 \cdot 10^4$
$9 \cdot 10^3$
$8 \cdot 10^3$
$7 \cdot 10^3$
$6 \cdot 10^3$
$5 \cdot 10^3$
$4 \cdot 10^3$
$3 \cdot 10^3$
$2 \cdot 10^3$
$1 \cdot 10^3$
0

Fig. 17

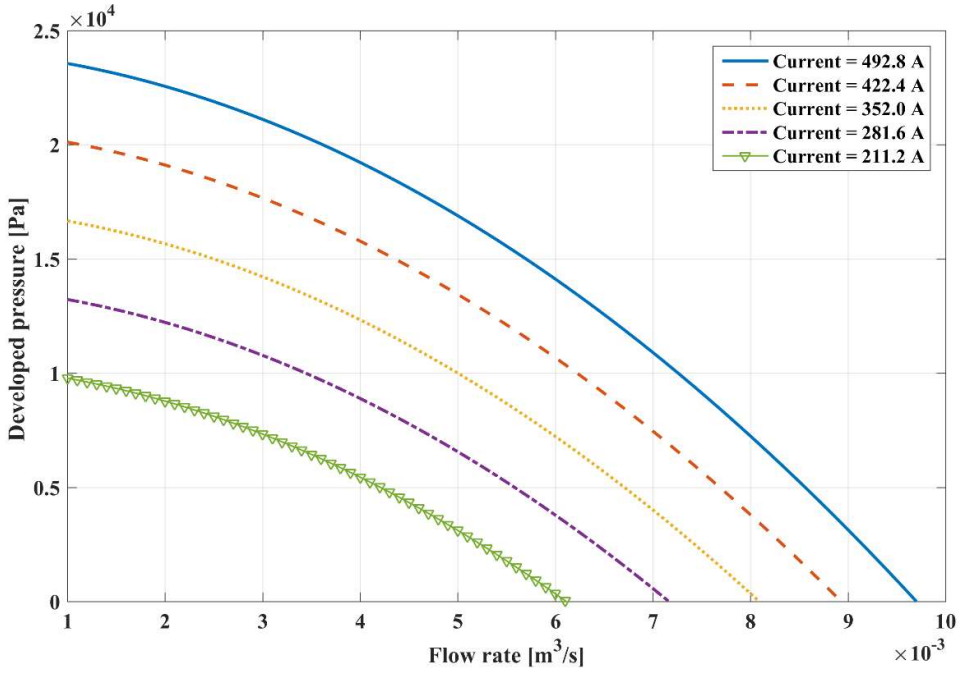
$\times 10^4$
2.5
2
1.5
1
0.5
0
Developed pressure [Pa]
1
2
3
4
5
6
7
8
9
10
$\times 10^{-3}$
Flow rate [m$^3$/s]
Current = 492.8 A
Current = 422.4 A
Current = 352.0 A
Current = 281.6 A
Current = 211.2 A

Fig. 18